Simulation studies of self-organization of microtubules and molecular motors

Zhiyuan Jia,[1,2] Dmitry Karpeev,[2] Igor S. Aranson,[3] and Peter W. Bates[1]
[1]*Department of Mathematics, Michigan State University, East Lansing, Michigan 48824, USA*
[2]*Mathematics and Computer Science Division, Argonne National Laboratory, 9700 South Cass Avenue, Argonne, Illinois 60439, USA*
[3]*Materials Science Division, Argonne National Laboratory, 9700 South Cass Avenue, Argonne, Illinois 60439, USA*
(Received 25 September 2007; revised manuscript received 17 January 2008; published 8 May 2008)

We perform Monte Carlo type simulation studies of self-organization of microtubules interacting with molecular motors. We model microtubules as stiff polar rods of equal length exhibiting anisotropic diffusion in the plane. The molecular motors are implicitly introduced by specifying certain probabilistic collision rules resulting in realignment of the rods. This approximation of the complicated microtubule-motor interaction by a simple instant collision allows us to bypass the "computational bottlenecks" associated with the details of the diffusion and the dynamics of motors and the reorientation of microtubules. Consequently, we are able to perform simulations of large ensembles of microtubules and motors on a very large time scale. This simple model reproduces all important phenomenology observed in *in vitro* experiments: Formation of vortices for low motor density and raylike asters and bundles for higher motor density.

DOI: 10.1103/PhysRevE.77.051905 PACS number(s): 87.16.Ka, 05.65.+b, 87.18.Hf

I. INTRODUCTION

Organization of complex networks of long biofilaments such as microtubules and actin filaments in the course of cellular processes and division is one of the primary functions of molecular motors [1]. A number of *in vitro* experiments were performed [2–7] to study the interaction of molecular motors and microtubules energized by the hydrolysis of adenosine triphosphate in isolation from other biophysical processes simultaneously occurring *in vivo*. The experiments clearly demonstrated that at large enough concentration of molecular motors and microtubules, the latter organize into raylike asters and rotating vortices depending on the type and concentration of molecular motors. These experiments spurred numerous theoretical studies addressing various aspects of self-organization of active filament systems [8–17].

The experiments [4–7] suggested the following qualitative picture of motor-filament interaction. After a molecular motor has bound to a microtubule at a random position, it marches along it in a definite direction until it unbinds without appreciable displacement of microtubules (since the size of a molecular motor is small in comparison with that of the microtubule). However, if a molecular motor binds to two microtubules [some molecular motors (e.g., kinesin) form clusters with at least two binding sites], it exerts significant torques and forces, and can change the positions and orientations of the microtubules significantly, leading eventually to the onset of large-scale ordered patterns.

Small-scale molecular dynamics simulations were performed to elucidate the nature of self-organization [4,5]. In these simulations the microtubules were modeled by semiflexible rods diffusing in viscous fluids. Molecular motors were correspondingly modeled by short stiff linear springs with a large diffusion coefficient. Once the motor diffuses to within a certain small distance from the intersection point of two microtubules, it attaches to them with a certain probability p_{on} and marches along with velocity v. The action of the motor is to exert forces and torques on the microtubules, resulting in their mutual displacement and realignment. Then, the motor detaches with a probability p_{off}. To model the dwelling effects of the motors on the end points of microtubules, observed for some types of molecular motors, an additional probability p_{end} to leave the end point was assigned. The corresponding typical dwelling time t_{end} is of the order $1/p_{\mathrm{end}}$. The simulations in [4,5] indeed reproduced certain features of the observed phenomenology, such as the stability of patterns and transitions between vortices and asters. However, in this approach many fundamentally different time scales had to be simultaneously resolved computationally (e.g., fast diffusion of the motors and very slow pattern formation). As a result, the method is very CPU intensive, and only a small number of microtubules were studied numerically, leaving many important questions, such as the nature of the transition and structure of the phase diagram, unanswered.

In Refs. [12,13] a continuum probabilistic model of alignment of microtubules mediated by molecular motors was developed. The theory was formulated in terms of a stochastic master equation governing the evolution of the probability density of microtubules with a given orientation at a given location. The theory is based on a number of simple assumptions on the interaction rules between microtubules and molecular motors. In particular, only binary instant interactions of microtubules called inelastic collisions are considered. These are mediated by molecular motors in a two-dimensional microtubule-motor mixture of constant motor density. The motors are implicitly introduced into the model by specifying the probability of interaction of intersecting microtubules. Despite all of the above simplifications of the biological process of self-organization of the cytoskeleton, the model reproduced, on a qualitative level, key experimental observations, such as the onset of an oriented (polar) phase above a critical density of motors, formation of asters for large density of motors and vortices for lower density, direct transition toward asters from the isotropic state for large dwelling times of the motors at the end of microtubules, and a density instability and the onset of bundle formation at very high motor density.

However, due to significant complexity of the derived stochastic master equation governing the evolution of the probability density of microtubules, the analysis in Refs. [12,13] was carried out in a relatively narrow range of parameters, namely, in the vicinity of the orientational instability, which allowed rigorous reduction of the stochastic master equation to a set of much simpler amplitude or Ginzburg-Landau-type equations for the local coarse-grained density and orientation of microtubules. This approach yields some important insights into the self-organization process, but, it obviously has its own limitations.

In this paper we perform Monte Carlo type simulation studies of self-organization of microtubules interacting with molecular motors. Instead of modeling the self-organization process in all details as was done in Refs. [4,5], we use simplified interaction rules suggested by our previous works [12,13]. This simplification allows the elimination of fast time scales associated with the diffusion and motion of the motors. Consequently, one may focus on relevant time and length scales associated with large-scale pattern formation and evolution. We studied very large ensembles of microtubules and addressed questions related to the structure of the corresponding phase diagram and the transitions between various patterns. In agreement with the early experiments, we were able to reproduce asterlike structures for a high motor density and vortices for a lower density, as well as transitions to bundles. Our approach provides direct access to the dynamics of the stochastic master equation and obtains insights far beyond the amplitude equations approach. Moreover, our method provides an efficient and fast tool for the simulation of a complex biological process of cytoskeleton self-organization and can be possibly extended to rather different systems, such as anisotropic granular media and systems of self-propelled particles.

II. ESSENTIALS OF THE MODEL

We model microtubules as stiff polar rods of equal length l exhibiting anisotropic diffusion in the plane. Diffusion of the rod is characterized by three diffusion coefficients, diffusion parallel to the rod orientation $D_{\|}$, perpendicular to its orientation $D_{\perp}$, and rotational diffusion D_r. In the following we assume $D_{\|}=2D_{\perp}$ [18] for stiff rods diffusing in a viscous fluid.

The key ingredient in the theory proposed in Refs. [12,13] was the approximation of the complicated process of interaction of molecular motors with two microtubules by a simple instant alignment process, see Fig. 1. We focus on the two-dimensional situation, and describe the orientation of microtubules by the planar angles $\varphi_{1,2}$. The microtubules before the collision possess initial angles $\varphi^b_{1,2}$. The action of the molecular motor binding simultaneously to two microtubules results in their mutual alignment, and the angles after interaction become

$$\varphi^a_1 = \varphi^a_2 = \frac{\varphi^b_1 + \varphi^b_2}{2}. \tag{1}$$

By analogy with the physics of inelastically colliding grains, we call this kind of process fully inelastic collision (see, e.g., [19]). Such an inelastic collision is a simple and reasonable approximation of the complicated interaction process [13], and is, in fact, an effect of simultaneous action of several motors or motors and static cross linking polymers. An analysis of the interaction of two stiff rods with one motor shows that the overall change in the angle between the rods is rather small: The angle decreases only by 25%–30% on average [13,14]. However, simultaneous action of a static cross link, serving as a hinge, and a motor moving along both filaments results in a fast and complete alignment of the filaments [20]. This justifies the assumption of fully inelastic and instantaneous collisions for the rods' interaction. Complete alignment also occurs for the case of a simultaneous action of two motors moving in the opposite directions, as in the experiments with kinesin and NCD (gluththione-S-transferase-nonclaret disjunctional fusion protein) mixtures [5]. The same is true of two motors of the same type moving in the same direction but with different speeds, where the variation in speed is due to the variability of motor properties and the stochastic character of the motion.

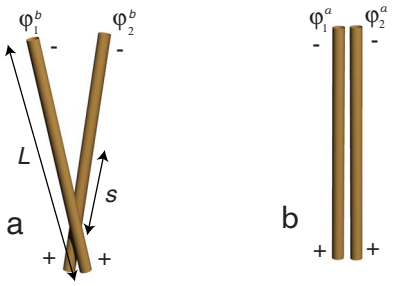

FIG. 1. (Color online) Schematics of an alignment event (inelastic collision) between two microtubules interacting with multiheaded molecular motors. (a) A multiheaded molecular motor cluster attached at the intersection point of microtubules moves from the positive (+) toward the negative (−) end of the microtubules. (b) After the interaction, the orientational angles $\varphi_{1,2}$ and the corresponding positions of the midpoints $\mathbf{R}_{1,2}$ become aligned.

The motor concentration m affects the probability of interaction P_{int} between two microtubules in a given period of time Δt. On scales larger than the microtubule length (the "macroscopic scale") the mean concentration of motors $\bar{m}$ is assumed to be constant. This simplifying assumption is justified by a strong motor diffusion D_m compared to the microtubule diffusion, $D_m \approx 20\ \mu\text{m}^2/\text{s} \approx 500 D_{\|}$.

Locally, on the "microscopic scale," the motor density deviates from the mean density $\bar{m}$ due to the advection of the motors along the microtubules so that motors are more likely to be found near the microtubules' polar ends (e.g., positive end for conventional kinesin). In particular, in the ordered phase this leads to motor accumulation at the centers of asters and vortices (see, e.g., [5,7]). This accumulation is likely more pronounced for NCD-type motors in Ref. [5] than for kinesin-type motors due to a larger dwelling time of the former on the ends of microtubules. While the accumulation of motors at the centers of asters and vortices also produces large-scale inhomogeneities of the motor distribution (i.e., deviations from a constant in $\bar{m}$), for the sake of simplicity we neglect these effects in our algorithm. There is some evidence that such large-scale inhomogeneities have only a

quantitative and no qualitative effect on the dynamics. In particular, the morphology of the phase transition diagram based on the amplitude equations (see [12,13]) is unaltered by the introduction of the macroscopic motor density variations.

The local motor density inhomogeneity affects the alignment rate in several ways, generally enhancing the probability of alignment for the rods intersecting near their positive ends for kinesin or negative ends for NCD motors [12,13]. To account for this, we assume that the interaction probability P_{int} depends on the position of the intersection point, see Fig. 1. The intersection position is indicated by the signed distance $s_{1,2}$, $-\frac{l}{2} \leq s_{1,2} \leq \frac{l}{2}$, from the midpoint of each rod.

The dependence of the interaction probability on the intersection (and, consequently, the attachment position) results in anisotropic interactions, corresponding to the anisotropy of the probability kernel in the collision integral of the master equation in [12,13]. This anisotropy is characterized by the parameter β, ranging between -1 and 1, and is best quantified by the motor dwelling time t_{end}, which is small for kinesin-type motors and large for NCD-type motors.

The reason that t_{end} is the controlling parameter for anisotropy is that larger dwelling times entail higher motor accumulation, by blockading subsequent motors near the tubule's end. Furthermore, by keeping the rods in an intersection configuration longer enhanced the probability of multiple cross-linking and, hence, a higher probability and a greater degree of alignment.

In Ref. [13] the relation between the kernel anisotropy β and the motor dwell time at the end of the microtubule t_{end} in the limit of $t_{\text{end}} \gg 1$ was estimated as follows: $\beta \sim (v - \text{const}/t_{\text{end}})/p_{\text{off}}$, where v is the motor speed, p_{off} is the motor unbinding rate. Thus, one sees that β increases with the increase in t_{end}. In contrast, the motor attachment rate p_{on} has little effect on the kernel anisotropy, in agreement with experiments [4,5,7]. As was shown in Refs. [12,13], the anisotropy parameter controls the transition between asters and vortices; in the continuum model no vortices were observed for large values of the kernel anisotropy.

In order to accommodate the discussed anisotropy effects in our model we introduce the following dependence of the interaction probability on the attachment positions:

$$P_{\text{int}} = P_0\left(1 + \beta\frac{s_1 + s_2}{l}\right). \tag{2}$$

Here $P_0 = C\bar{m}\sigma^2\Delta t$, which encodes the aforementioned dependence of the interaction probability on the macroscopic motor concentration $\bar{m}$, the interaction cross section σ, and the elapsed time Δt (C is a constant). The value of $\sigma \approx 30-50$ nm is the order of size of a kinesin-type molecular motor. Since σ is a fixed physical parameter, and Δt is fixed throughout our simulations (see below), the range of parameter values $0 < P_0 \leq 0.5$ reflects different values of the uniform coarse-grained motor concentration $\bar{m}$. The value (and the sign) of the other parameter, β, depends on the type of motor. We believe that this generic linear dependence on the distances $s_{1,2}$ captures the qualitative effects of the kernel anisotropy. Our experiments with different dependencies of the probability P_{int} on $s_{1,2}$ yielded qualitatively similar results.

After the interaction we postulate that not only the angles, but also the midpoint positions of the microtubules $\mathbf{R}_{1,2}$, coincide

$$\mathbf{R}_1^a = \mathbf{R}_2^a = \frac{\mathbf{R}_1^b + \mathbf{R}_2^b}{2}. \tag{3}$$

This approximation is reasonable in the case of large dwelling times t_{end} of the motors, which guarantees that after the interaction the end points of the microtubules will coincide. Then, together with the alignment interaction, this effect will justify the assumption on the alignment of the midpoints as well. A large value of the dwelling time t_{end} is a reasonable approximation for NCD motors; however, t_{end} is small for kinesin-type motors. As we will show later, the midpoint alignment assumption may produce under some conditions specific effects, such as layering of the microtubules, or "smectic ordering" [21]. In our future work we plan to introduce more realistic rules for the midpoint displacements.

III. ALGORITHM DESCRIPTION

We performed simulations on a two-dimensional square domain with periodic boundary conditions. Initially, microtubules are randomly distributed over the domain. At each time step (e.g., from t_n to t_{n+1}), the update of the positions and orientations of the microtubules is comprised of one substep processing anisotropic diffusion and one substep processing inelastic collision. The total time-step size was set at $\Delta t = 0.1$.

The diffusion of rigid rods in a viscous fluid is characterized by three diffusion coefficients: parallel $D_{\parallel}$, perpendicular $D_{\perp}$, and rotational D_r. We used the following relations between the diffusion coefficients from Kirkwood's theory for polymer diffusion in three dimensions: $D_{\parallel} = 2D_{\perp}$, $D_r = \frac{c}{l^2}D_{\parallel}$. We used $c = 1.5$ and $l = 0.5$ in our simulation [22]. The "diffusion substep" is introduced as an anisotropic random walk of the microtubules' center position $\mathbf{R} = (x, y)$ and random rotation of its orientation φ. The positions and orientations are updated at each such substep as follows:

$$\mathbf{R}_{n+1} = \mathbf{R}_n + \zeta_1\Delta_{\parallel}\mathbf{U}_n + \zeta_2\Delta_{\perp}\mathbf{N}_n,$$

$$\varphi_{n+1} = \varphi_n + \zeta_3\Delta_r, \tag{4}$$

where $\zeta_i \in (-0.5, 0.5)$ are three uniform random numbers generated each time, and $\Delta_i = \sqrt{24 D_i \Delta t}$, where D_i is either $D_{\perp}, D_{\parallel}$ or D_r, and vectors $\mathbf{U}_n = (\cos\varphi_n, \sin\varphi_n)$, $\mathbf{N}_n = (-\sin\varphi_n, \cos\varphi_n)$ are directed along ($\mathbf{U}$) and perpendicular ($\mathbf{N}$) to the orientation of the microtubule. The factor 24 in the expression for Δ_i ensures that the effective diffusion has the correct value of D_i based on the variance of ζ_i.

At the "collision step," after diffusion, we check whether any pairs of microtubules intersect, and if so we locate the intersection points of the microtubules and assign an interaction probability to those pairs according to (2). In all of those intersections, some of them are simple binary intersections, but others may be multiple intersections, that is, a microtu-

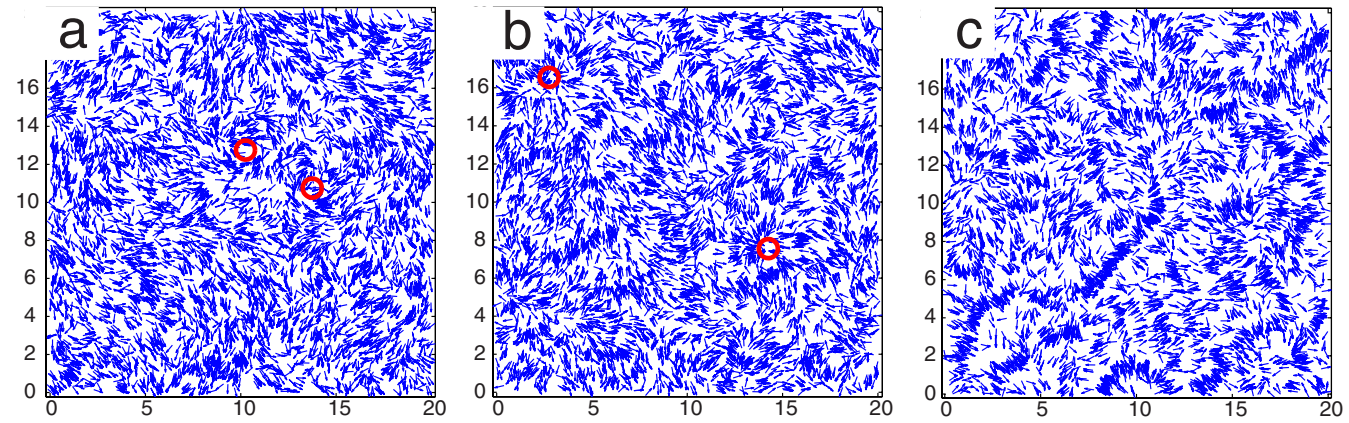

FIG. 2. (Color online) Snapshots illustrating configuration of 6000 rods for different motor densities, i.e., different values of P_0. Arrows represent microtubules, circles depict the cores of vortices or asters. (a) Vortices, $t=620$, $\beta=1.0$, $P_0=0.08$ (low motor density); (b) asters, $t=602$, $\beta=0.95$, $P_0=0.10$ (high motor density); (c) bundles, $t=400$, $\beta=1.0$, $P_0=0.15$. See also [23] for movies Nos. 1 and 2 illustrating the self-organization process.

bule intersecting with more than one other microtubule. Certainly, at a low density of microtubules binary collisions are more typical. Regardless of whether intersections are binary or multiple, we calculate all interaction probabilities and sort them in descending order. Starting with the greatest P_{int}, we compare it with a randomly generated number $\zeta_4 \in [0,1]$. If $P_{\text{int}} > \zeta_4$, then we update that pair of microtubules according to the collision rules, Eqs. (1) and (3). If either of these two microtubules have other intersections, they are ignored, that is, these interaction probabilities are set to zero. We then proceed with the next largest interaction probability, repeating until all have been acted upon. Note that the diffusive substep size coincides with the total time-step size, so that collisions are assumed to take place instantaneously.

Coarse-grained variables. In our simulations, the rods move freely within the domain and with fluctuations in both position and orientation of the rods, it is difficult to identify relatively stable patterns. For this reason, and as an aid for computing divergence and curl, we impose a square grid on the domain with the mesh length d and introduce a coarse-graining procedure to extract observable values, such as the local orientation τ and local density ρ. Using $\mathbf{W}$ to denote the two-dimensional position vector of a grid point (X_i, Y_j), we calculate the number of rods N whose midpoint positions are in the box $[X_i-d, X_i+d]\times[Y_j-d, Y_j+d]$. The following coarse-grained functions are employed to compute τ and ρ at this grid point (X_i, Y_j):

$$\tau(\mathbf{W}) = \frac{\sum_{k=1}^{N} \Phi(|\mathbf{W}-\mathbf{R}_k|)\mathbf{U}_k}{\left|\sum_{k=1}^{N} \Phi(|\mathbf{W}-\mathbf{R}_k|)\mathbf{U}_k\right|},$$

$$\rho(\mathbf{W}) = N. \tag{5}$$

Here $|\cdots|$ is Euclidean length and Φ is a weighting function. We take

$$\Phi(s) = e^{-s^2/l^2}, \tag{6}$$

where l is chosen to be the length of each microtubule. In the simulation we also must include contributions from "image particles" originating from the periodic boundary conditions.

IV. SIMULATION RESULTS

We applied our model to 6000 microtubules in a 20×20 domain varying parameters P_0 and β in a wide range with 7000 time steps in the simulation for each choice of (P_0, β). We impose a 40×40 grid on the domain to calculate the coarse-grained field. A snapshot was taken every 10 iterations and so 700 snapshots were obtained for each simulation process. For most of the parameter values chosen, it took about 300 snapshots (3000 time steps) to relax toward relatively stable large scale patterns, and more than 500 snapshots (5000 steps) to become stationary. The movies illustrating typical simulation results can be found in [23]. Some simulations clearly showed a pattern of asters and/or vortices while others resulted in ambiguous patterns. Moreover, the clear-cut distinction between asters and vortices appears to be difficult because of fluctuations. To examine the parameter space (P_0, β) where there are transition regions between asters and vortices, we have devised a pattern characterization scheme. The simulation results obtained from the first 4000 iterations were ignored as they represent transient states. The details of the pattern characterization procedure are presented in the Appendix.

Select simulation results are shown in Figs. 2–4 where $D_{\parallel}=1/120$ in all simulations. In agreement with the experiments [4,5] and the theoretical models [12,13], we obtained an isotropic phase for low motor densities (not shown), and then vortices, transient aster-vortices (structures which resemble vortices near the core and aster far from the core), asters, and bundles with gradual increase of the motor density. Representative snapshots of the rod configurations for three different values of the motor density P_0 are shown in Fig. 2 and the two corresponding coarse-grained snapshots of them superimposed with the rod density field are shown in

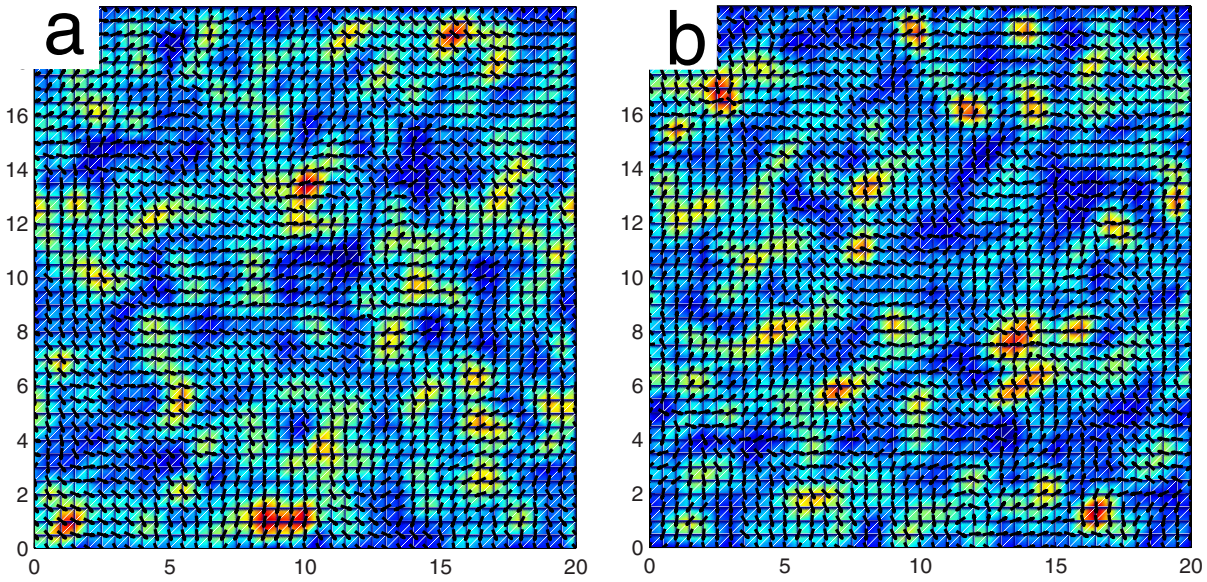

FIG. 3. (Color online) Coarse-grained images corresponding to parameters of Fig. 2 for vortices (a) and asters (b). Arrows represent the orientation field τ. The color (gray levels) shows the density ρ, red (bright) corresponds to the maximum of ρ, and blue (dark) to its minimum. See also [23] for movies Nos. 3 and 4.

Fig. 3. As is evident from our simulation results, a transition from an isotropic (disordered) phase to an oriented phase happens with the increase in the motor density characterized by the parameter P_0. While due to the small size of the system (only 6000 particles) we have very strong fluctuations in the number of vortices, asters and antiasters (structures similar to asters but with the opposite orientation of microtubules; see Fig. 4), a general trend can be identified: With the increase in the interaction probability P_0 the average number of vortices decreases while the number of aster increases. For small values of the anisotropy parameter β, asters and antiasters appear to occur with equal probability. However, with the increase in β the number of antiasters

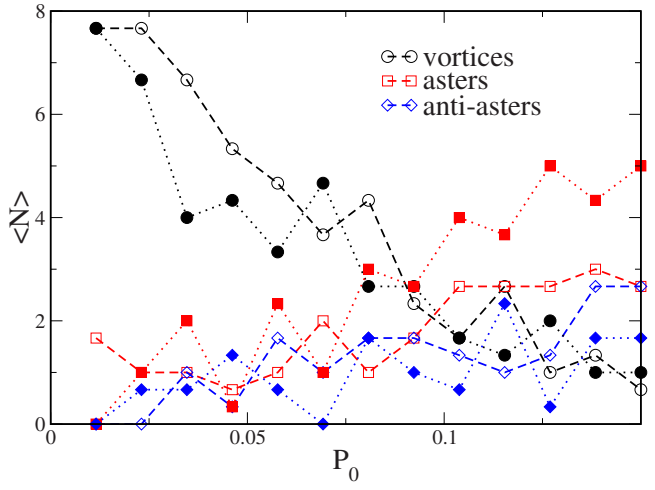

FIG. 4. (Color online) Averaged number of asters (squares), antiasters (diamonds), and vortices (circles) as a function of the interaction probability P_0 for two different values of parameter β. The data for β=0.35 are shown with dashed lines, open symbols, and for β=0.95 are shown with dotted lines, closed symbols.

rapidly decreases while the number of asters increases. For very high motor densities we observed an additional instability resulting in the formation of dense bundles of filaments with the same orientation [see Fig. 2(c)]. The bundles are also associated with a certain layering (smectic ordering) of the filaments. This ordering is due to the microscopic interaction law which results in the alignment of the rod midpoints as in Eq. (3). While this might be the case for the NCD motors with a large dwelling time, for the kinesin motors the bundles may have a different structure which is not necessarily captured by these simulations. These results are in good agreement with earlier theoretical predictions [12,13].

The phase diagram delineating various regimes of self-organization is shown in Fig. 5. It bears a strong resemblance to the experimental observations [4,5] and the theoretical model of Refs. [12,13]. While the boundaries are quite blurred due to strong fluctuations (see Fig. 4), there is a transition from vortices to asters with the increase of the interaction rate P_0 [24]. Moreover, the domain of stability of vortices decreases with the increase of the anisotropy parameter β related to the dwell time of the motors, as observed experimentally and in agreement with the continuum model of Refs. [12,13]. However, we need to emphasize that all the boundaries shown in Fig. 5 are rather blurred; instead of sharp phase transitions we observed only smooth crossovers between different regimes due to strong fluctuations and a relatively small number of particles in the system [25].

The coarse graining allows for easier identification of aster and vortex structures (see Fig. 3). In the movies made using coarse-grained fields we are able to follow the formation, interaction, and evolution of asters and vortices. A typical scenario of the dynamical evolution of the system is that small vortices and asters can coalesce to form a larger vortex or aster (see the movies in [23] for parameters P_0=0.12, β =1.0). In accordance with the experiments, vortices have

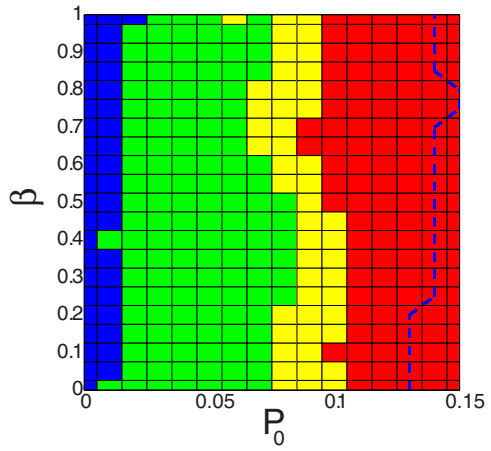

FIG. 5. (Color online) Phase diagram of various regimes as the function of the motor density P_0 and the anisotropy parameter β. The disordered region is blue (black) here; the vortex region is green (gray); the transition from vortex to aster happens at the yellow region (white); and red (dark gray) denotes aster regions. The dashed line denotes the boundary where the rods become bundled.

suppression of the microtubule density in the center (holes) and asters lead to an increase of the density of microtubules. We have also observed the transformation of vortices into asters in the course of the simulations, likely due to fluctuation and finite size effects.

We followed the trajectory of individual rods in the vicinity of the vortex core in the steady state. We have found that the particles generally do not rotate around the vortex core. This stems from the fact that in our binary collision algorithm the center of mass of two interacting rods is not displaced in the course of collision, Eq. (3). This restriction suppresses directed motion of the rods, and, consequently, global rotation. Thus, the rotation of microtubules seen in experiment [4] is likely related to the interaction with the substrate or the boundary of the container [13,17], or, possibly is related to multiparticle interactions and anisotropic interaction with the fluid [11] neglected in our model.

In our simulations we also observed that the centers of the asters typically exhibit a drift, reminiscent to the acceleration instability of aster cores predicted in Ref. [13]. This phenomenon especially appears at the stage of formation of asters. However, the precise nature of the drift is still an open question since it could be also due to fluctuation effects.

V. CONCLUSION

In this paper we developed a Monte Carlo type stochastic approach to the study of self-organization of microtubules mediated by molecular motors. The approach allows us to bypass the fast time scales associated with the diffusion and the motion of individual molecular motors and concentrates on the relevant features of the long-time and large-scale behaviors associated with the self-organization phenomena.

While a direct comparison with the earlier algorithms introduced in Ref. [7] is not always possible due to the different nature of the approximations, some rough estimates are useful. The total simulation time reported in Ref. [7] was 1500 s. The characteristic time scale of the simulations of the order of 1 s can be inferred from the density of microtubules (about 0.05 μm^{-2}, or about 500 microtubules in a box 100 $\times$100 microns) and the motor diffusion (D=20 $\mu m^2/s$), which roughly corresponds to 10^3 dimensionless units of time. Our simulations [26], with much higher number of microtubules (6000) and in bigger boxes, were performed for about 1000 dimensionless time units, that is, about the same order of magnitude as in Refs. [4,7].

Our method can be easily adapted to new experimental settings, such as a motor and microtubule system with a fraction of the motors permanently bound to the substrate [17]. Our results are complementary to the analytical studies of self-organization in the framework of amplitude equations derived from the stochastic master equations, and provide valuable tests for a variety of phenomenological continuum theories of cytoskeleton formation [8–11,16]. Moreover, our simulations shed light on the microscopic details of self-organization not available in the continuum formulation. We anticipate that somewhat similar approaches can be applied to a broad range of systems, such as networks of actin filaments interacting with myosin motors [6], patterns emerging in granular systems with anisotropic particles [27–31], and systems of self-propelled objects [32–34].

ACKNOWLEDGMENTS

We thank Lev Tsimring, Jacques Prost, Francois Nédélec, Falko Ziebert, and Walter Zimmermann for useful discussions. This work was supported by the U.S. Department of Energy Grant No. DE-AC02-06CH11357, and in part by NSF Grant No. DMS-0401708 and DARPA Grant No. FunBio HR 0011-05-1-0057.

APPENDIX: PATTERN CHARACTERIZATION

We computed the discrete divergence, $\mu=\nabla\cdot\tau$, and the curl, $\omega=\nabla\times\tau$, of the coarse-grained field of the pattern from the last 3000 iterations. Here μ and ω depend on the mesh size of the coarse-grained field. By using the central difference scheme, the extrema of μ and ω can be -4 or 4 for an ideal aster or vortex under the 40×40 grid on the 20×20 domain.

The basic idea for pattern characterization is that an aster would have its local divergence greater or less than a threshold value at the center. Similar observations apply to a vortex and its curl. To realize the pattern characterization, we implemented the following procedures:

(i) First, using the snapshot at t=700, determine the local extrema of μ and ω with values sufficiently far from zero. Specifically,

(1) compute the minimal value of the divergence μ. Suppose that it occurs at (i,j);

(2) eliminate the surrounding square area consisting of $(2q+1)\times(2q+1)$ mesh points. We choose q=4 in our computation, that is, temporarily set $\mu(k,l)=0$, $i-4\le k\le i+4$, $j-4\le l\le j+4$. Locate the next minimal value of μ from the remaining region;

(3) repeat step (2) on the remaining region until $\mu > -2.5$;

(4) use the above three steps to find the maxima of μ with $\mu > 2.5$;

(5) go through steps (1)–(3) to locate the local minima of ω with $\omega < -2.5$;

(6) apply a similar procedure to find local maxima of ω with $\omega > 2.5$;

(7) if two of the selected extrema of $|\mu|$ and $|\omega|$ occur in one of the selected squares, then we discard the square that is not centered at a point where the greater of $|\mu|$ and $|\omega|$ occurs.

(ii) Second, take the local square area consisting of $(2q+1)\times(2q+1)$ mesh points for each of the extracted locations, and compute four quantities, $\mu_{\min}$, $\mu_{\max}$, $\omega_{\min}$ and $\omega_{\max}$ in this patch for each snapshot from $t=401$ to $t=700$.

(iii) Third, compute the time averages of those four quantities for each patch from these 300 snapshot values, denoted as $\bar{\mu}_{\min}=\frac{1}{300}\Sigma_{i=1}^{300}|\mu_{\min}(i)|$, $\bar{\mu}_{\max}=\frac{1}{300}\Sigma_{i=1}^{300}\mu_{\max}(i)$, $\bar{\omega}_{\min}=\frac{1}{300}\Sigma_{i=1}^{300}|\omega_{\min}(i)|$, and $\bar{\omega}_{\max}=\frac{1}{300}\Sigma_{i=1}^{300}\omega_{\max}(i)$. To distinguish between a vortex and an aster, we introduced an additional parameter $\xi=0.6$, whose use is explained below.

(iv) Finally, to determine the type of pattern in each local square area, according to the following criteria, we decide

(a) if $\bar{\mu}_{\min}\geq 3.0$, $\bar{\omega}_{\max}<3.0$, $\bar{\omega}_{\min}<3.0$, and $\bar{\mu}_{\max}\leq\xi\bar{\mu}_{\min}$, it is an aster;

(b) if $\bar{\mu}_{\min}\geq 3.0$, $\bar{\omega}_{\max}\geq 3.0$ $(\bar{\omega}_{\min}\geq 3.0)$, $\bar{\omega}_{\min}\leq\xi\bar{\mu}_{\min}$ $(\bar{\omega}_{\max}\leq\xi\bar{\mu}_{\min})$, and $\bar{\mu}_{\max}\leq\xi\bar{\mu}_{\min}$, it is an intermediate form between an aster and a vortex and we assign it an aster-vortex pattern;

(c) if $\bar{\mu}_{\max}\geq 3.0$, $\bar{\omega}_{\max}<3.0$, $\bar{\omega}_{\min}<3.0$, and $\bar{\mu}_{\min}\leq\xi\bar{\mu}_{\max}$, the directions of the rods point outward and it is an antiaster pattern;

(d) if $\bar{\mu}_{\max}\geq 3.0$, $\bar{\omega}_{\max}\geq 3.0$ $(\bar{\omega}_{\min}\geq 3.0)$, $\bar{\omega}_{\min}\leq\xi\bar{\mu}_{\max}$ $(\bar{\omega}_{\max}\leq\xi\bar{\mu}_{\max})$, and $\bar{\mu}_{\min}\leq\xi\bar{\mu}_{\max}$, it is an antiaster-vortex pattern;

(e) if $\bar{\mu}_{\min}<3.0$ and $\bar{\mu}_{\max}<3.0$ and $\bar{\omega}_{\min}\geq 3.0$ $(\bar{\omega}_{\max}\leq\xi\bar{\omega}_{\min})$ or $\bar{\omega}_{\max}\geq 3.0$ $(\bar{\omega}_{\min}\leq\xi\bar{\omega}_{\max})$, then it is a vortex pattern;

(f) in any other case, it is isotropic.

The parameter space (P_0,β) is in the range $0.01\leq P_0\leq 0.15$ and $0.0\leq\beta\leq 1.0$. We made a grid with step sizes $\Delta P_0=0.01$ and $\Delta\beta=0.05$ so that we had $15\times 21=315$ mesh points. For each pair of values, we used three different initial conditions for the simulations, using the characterization of the final states described above. We obtained the numbers of asters N_a, aster vortices N_{av}, antiasters N_{aa}, antiaster vortices N_{aav}, and vortices N_v for each (P_0,β) and we found that $N_{aa}=0$ and $N_{aav}=0$. At each parameter grid point we computed two values according to the following formulas:

$$M_a(i,j)=\frac{1}{N_1}\sum_{i-1}^{i+1}\sum_{j-1}^{j+1}(N_a+N_{aa}), \tag{A1}$$

$$M_v(i,j)=\frac{1}{N_1}\sum_{i-1}^{i+1}\sum_{j-1}^{j+1}(N_v). \tag{A2}$$

For the boundary points, the summations in (A1) and (A2) are taken only over the neighboring points around (i,j) within the parameter domain. N_1 in (A1) and (A2) is the number of points in the summation. From $M_a(i,j)$ and $M_v(i,j)$, we calculated $\gamma_a(i,j)=\frac{M_a(i,j)}{M_a(i,j)+M_v(i,j)}$ and $\gamma_v(i,j)=\frac{M_v(i,j)}{M_a(i,j)+M_v(i,j)}$. Finally we generated a matrix, I_p, whose entries give the pattern information at that parameter point.

(i) If $\frac{1}{3}[M_a(i,j)+M_v(i,j)]\leq 1.5$, then it belongs to a disordered region and $I_p(i,j)=-1.0$.

(ii) If $\gamma_a(i,j)\geq 0.6$ and $\gamma_v(i,j)\leq 0.4$, then it belongs to an aster region and $I_p(i,j)=1.0$.

(iii) If $\gamma_a(i,j)\leq 0.4$ and $\gamma_v(i,j)\geq 0.6$, then it belongs to a vortex region and $I_p(i,j)=0.0$.

(iv) Otherwise, it belongs to a transition region and $I_p(i,j)=0.5$.

We used the I_p matrix to produce a pseudocolor phase diagram. The pixels with $I_p(i,j)=1$ are assigned red, the pixels with $I_p(i,j)=0.5$ are assigned yellow, the pixels with $I_p(i,j)=0.0$ are assigned green, and the pixels with $I_p(i,j)=-1.0$ are assigned blue.

To identify the bundled region, we calculated the density of the rods at each grid point, which is defined as the number of rods whose positions are in the square box with the grid point as the center. Next we computed the global minimal and maximal density in the domain at each time slice. Those minimal and maximal densities were averaged over 300 slices and then over three samples, i.e., $\bar{\rho}_{\min}=\frac{1}{3}\Sigma_1^3[\frac{1}{300}\Sigma_{j=1}^{300}\rho_{\min}(j)]$, $\bar{\rho}_{\max}=\frac{1}{3}\Sigma_1^3[\frac{1}{300}\Sigma_{j=1}^{300}\rho_{\max}(j)]$. If $\bar{\rho}_{\min}<0.2$ and $\bar{\rho}_{\max}>60$, then this point is marked bundled. In the bundled region the rods formed several, with these stripes sometimes forming concentric circles. Moreover, asters appear to dominate vortex structures.

[1] J. Howard, *Mechanics of Motor Proteins and the Cytoskeleton* (Springer, New York, 2000).

[2] K. Takiguchi, J. Biochem. (Tokyo) **109**, 250 (1991).

[3] R. Urrutia, M. A. McNiven, J. P. Albanesi, D. B. Murphy, and B. Kachar, Proc. Natl. Acad. Sci. U.S.A. **88**, 6701 (1991).

[4] F. J. Nédélec, T. Surrey, A. C. Maggs, and S. Leibler, Nature (London) **389**, 305 (1997).

[5] T. Surrey, F. Nédélec, S. Leibler, and E. Karsenti, Science **292**, 1167 (2001).

[6] D. Humphrey, C. Duggan, D. Saha, D. Smith, and J. Käs, Nature (London) **416**, 413 (2002).

[7] F. Nédélec, T. Surrey, and A. C. Maggs, Phys. Rev. Lett. **86**, 3192 (2001).

[8] H. Y. Lee and M. Kardar, Phys. Rev. E **64**, 056113 (2001).

[9] J. Kim, Y. Park, B. Kahng, and H. Y. Lee, J. Korean Phys. Soc. **42**, 162 (2003).

[10] T. B. Liverpool and M. C. Marchetti, Phys. Rev. Lett. **90**, 138102 (2003).

[11] K. Kruse, J. F. Joanny, F. Jülicher, J. Prost, and K. Sekimoto, Phys. Rev. Lett. **92**, 078101 (2004).
[12] I. S. Aranson and L. S. Tsimring, Phys. Rev. E **71**, 050901(R) (2005).
[13] I. S. Aranson and L. S. Tsimring, Phys. Rev. E **74**, 031915 (2006).
[14] D. Karpeev, I. S. Aranson, L. S. Tsimring, and H. G. Kaper, Phys. Rev. E **76**, 051905 (2007).
[15] F. Ziebert and W. Zimmermann, Eur. Phys. J. E **18**, 41 (2005).
[16] R. Voituriez, J. F. Joanny, and J. Prost, Phys. Rev. Lett. **96**, 028102 (2006).
[17] P. Kraikivski, R. Lipowsky, and J. Kierfeld, Phys. Rev. Lett. **96**, 258103 (2006).
[18] M. Doi and S. F. Edwards, *The Theory of Polymer Dynamics* (Clarendon, Oxford, 1988).
[19] I. S. Aranson and L. S. Tsimring, Rev. Mod. Phys. **78**, 641 (2006).
[20] F. Ziebert, I. S. Aranson, and L. S. Tsimring, New J. Phys. **9**, 421 (2007).
[21] P.-G. de Gennes and J. Prost, *The Physics of Liquid Crystals* (Clarendon, Oxford, 1995).
[22] For a three-dimensional fluid the coefficient $c \approx 24$ [18]. However, the value of c rapidly decreases for quasi-two-dimensional thin film and membranes, see, e.g., A. J. Levine, T. B. Liverpool, and F. C. MacKintosh, Phys. Rev. E **69**, 021503 (2004). We verified that the value of coefficient c does not change the qualitative behavior of the system, it affects only the position of the transition points.
[23] See EPAPS Document No. E-PLEEE8-77-016805 for computer animations of simulation results. For more information on EPAPS see http://www.aip.org/pubservs/epaps.html.
[24] Due to strong fluctuations, pattern characterization is rather difficult, and even sometimes ambiguous. In particular, we often observed antiaster, i.e., structures with the orientation of rods opposite to that determined by the motion of the motors. Thus, when we calculated the phase diagram, we had to take into account the number of antiasters and antiaster vortices. We also noticed that the rod density in aster regions is greater than that in antiaster regions. Specifically we found that there were about 80 more rods on average in an aster region than in an antiaster region.
[25] It is known that in related two-dimensional *XY* models there is no well-defined second-order phase transition from isotropic to ordered phase; the mechanism is related to unbinding of Kosterlitz-Thouless vortices by fluctuations, see, e.g., R. Gupta, J. DeLapp, G. G. Batrouni, G. C. Fox, C. F. Baillie, and J. Apostolakis, Phys. Rev. Lett. **61**, 1996 (1988). However, sharp phase transition occurs in three dimensions.
[26] Our numerical procedure, implemented in Fortran90, took approximately 69 minutes to complete each simulation (7000 steps with 6000 rods) on a 1.6 GHz Itanium2 machine with 4 GB of RAM.
[27] D. L. Blair, T. Neicu, and A. Kudrolli, Phys. Rev. E **67**, 031303 (2003).
[28] A. Kudrolli, G. Lumay, D. Volfson, and L. S. Tsimring, Phys. Rev. Lett. **100**, 058001 (2008).
[29] I. S. Aranson and L. S. Tsimring, Phys. Rev. E **67**, 021305 (2003).
[30] V. Narayan, N. Menon, and S. Ramaswami, J. Stat. Mech.: Theor. Exp. (2006) P01005.
[31] I. S. Aranson, D. Volfson, and L. S. Tsimring, Phys. Rev. E **75**, 051301 (2007).
[32] T. Vicsek, A. Czirók, E. Ben-Jacob, I. Cohen, and O. Shochet, Phys. Rev. Lett. **75**, 1226 (1995).
[33] G. Grégoire and H. Chaté, Phys. Rev. Lett. **92**, 025702 (2004); H. Chaté, F. Ginelli, and R. Montagne, *ibid.* **96**, 180602 (2006).
[34] D. Grossman, I. S. Aranson, and E. Ben-Jacob, New J. Phys. **10**, 023036 (2008).